Proceedings of ASME Turbo Expo 2019
GT2019
June 17–21, 2019, Phoenix, Arizona, USA

GT2019-91972

LIQUID JET IN CROSSFLOW : EFFECT OF MOMENTUM FLUX RATIO ON SPRAY AND VAPORIZATION CHARACTERISTICS

Manu Kamin, Prashant Khare
Department of Aerospace Engineering and Engineering Mechanics
University of Cincinnati, Cincinnati, 45221-0070, USA
Email: kaminms@mail.uc.edu, prashant.khare@uc.edu

ABSTRACT

A comprehensive study is conducted to identify the effects of momentum flux ratio on the spray and vaporization characteristics of liquid jet injected in air crossflow at elevated temperatures, a configuration relevant to high-speed propulsion systems, such as ramjets and afterburners. The physical setup consists of a straight chamber with a triangular bluff body downstream of the liquid injection location. The numerical simulations are based on an Eulerian - Lagrangian framework, where the gas phase flow behaviors such as recirculation zones, turbulence statistics, mixing of vaporized liquid and gas streams are resolved by solving the complete set of three-dimensional conservation equations of mass, momentum, energy and species, and the liquid phase is treated using the blob approach and tracked in a Lagrangian coordinate system. Turbulence closure is achieved using Large Eddy Simulation (LES) technique. Primary breakup of the liquid jet is simulated using the K-H wave breakup model, and the Taylor Analogy Breakup (TAB) model is used for secondary breakup. Two-way coupling between the liquid and gas phases is implemented in the LES framework to systematically model the exchange of mass, momentum and energy between the two phases. The formulation is validated against experimental measurements of liquid jet penetration and sauter mean diameter for a Weber number of 68 and momentum flux ratio of 9 at two temperatures, 298K and 573K. Results show excellent agreement with measurements for both cases. Next, simulations are conducted for a range of momentum flux ratios from 10-140 to identify the detailed gas and spray fields for vaporizing flow cases. This study helps to estimate the penetration of the liquid jet, droplet distribution, and then, location of the core of evaporated liquid in the gas-phase are quantitatively identified.

NOMENCLATURE

U : velocity
ρ : density
σ : surface tension
μ_a : Air viscosity μ_a
q : momentum flux ratio - $\rho_j u_j^2/\rho_a u_a^2$
We : Weber number - $\rho_a u_{rel}^2 D/\sigma$
Re_D : Jet Reynolds number - $\rho_a u_a D/\mu_a$

Subscripts:
D : Droplet diameter
a : inflow air
j : liquid jet
d : droplet phase

INTRODUCTION

Combustion in liquid fueled propulsion devices such as gas turbines, rockets and afterburners involve a series of complex phenomena, including primary and secondary atomization of the liquid fuel, vaporization, mixing, ignition, ensuing combustion and flame stabilization. Among all the physical processes, atomization and subsequent spray dynamics is especially important because the system performance is conditioned by the fuel droplet size distribution, which is often the rate-controlling process. A commonly used atomization technique in afterburners and ramjet engines consists of the liquid fuel being injected

perpendicular to an incoming air crossflow, with a v-gutter bluff body downstream of the fuel injector. While a number of experiments and a few numerical simulations studies have been conducted in the past to study atomization characteristics of liquid jets in such a configuration, a systematic study that details the effect of momentum flux ratio on atomization and vaporization behaviors of jet fuels is yet to be conducted. This is the focus of the current research effort.

Spray characteristics for a liquid jet injected into a crossflow of air have been studied extensively through experiments. Based on such measurements, correlations have been developed to predict the atomization behavior as a function of non-dimensional quantities, such as momentum flux ratio, Weber number and Reynolds number. For instance, Wu et al. [1] developed correlations to predict the height of liquid column over a range of momentum flux ratios and injector diameters based on experimentally obtained data. While such correlations are useful as a first estimate of trajectories of liquid jets, more detailed studies are necessary to be able to understand the spray characteristics better. Recently, Amighi et al. [2] performed experiments where water was injected into crossflowing air over a wide range of momentum flux ratio that varied from 8 to 298 at elevated temperature and pressure conditions. Global measurements of droplet sizes were reported for each case, and trends of variation of droplet sizes with liquid injection velocity, inflow air velocity and inflow air pressure. were identified. Although a global estimate of droplet sizes can be a very useful statistic, measurements that show spatial variation of droplet sizes provide far greater insight into the details of atomization process and droplet distribution. Many other studies have also been conducted in the past, that report similar correlations and trends [3–5]. Experimental measurements have also been conducted to measure concentration of vaporized liquid in the gas phase for cases at elevated inflow air temperature [6,7].

Apart from experiments, numerical simulations have also been conducted, although with varying degree of accuracy. One of the earliest attempts was made by Liu et al. [8], where multiple models for prediction of droplet breakup were used, and predicted jet penetration depth was compared with experiments. Gas phase equations were not solved. More sophisticated simulations were carried out by Madabhushi et al. [9]. Here, conservation equations were solved for the gas phase with models incorporated to predict the jet breakup, droplet kinematics and droplet sizes. However, interactions between the gas phase and liquid phase were ignored, leading to poor predictions of droplet velocities. No results were reported for the gas phase. Recently, Yoo et al. [10] performed LES calculations for liquid jet in crossflow. Mutual interaction between the droplets and freestream were considered. While the spray characteristics were studied systematically over a large range of momentum flux ratio and inflow air temperature, its influence on the flowfield was not investigated in detail.

The present study aims to address some of the shortcomings described above. A comprehensive, high fidelity analysis detailing the effects of momentum flux ratio on the spatio-temporal evolution of gaseous and spray fields, and associated statistics of liquid jet in vitiated air crossflow is presented using a large eddy simulation (LES) based framework.

Rest of the paper is organized in 5 sections. Section 2 details the theoritical framework and numerical methods. This is followed by section3, dedicated to model validation. Section4 describes the effect of momentum flux ratio on the carrier and discrete phases in terms of recirculation zones, droplet size distribution and the penetration of vaporized liquid mass fractions.

THEORITICAL FORMULATION AND NUMERICAL METHODOLOGY

The gaseous phase is formulated in the Eulerian frame, based on three-dimensional compressible form of conservation equations for mass, momentum, energy and species transport. Source terms appear in these equations due to phase transformation (and chemical reactions), and interactions between the continuous and and discrete phases. Turbulence closure is achieved by large eddy simulation technique. The conservation equations can thus be written as follows :

$$\frac{\partial \bar{\rho}}{\partial t} + \frac{\partial (\bar{\rho}\tilde{u_j})}{\partial x_j} = \dot{m^s} \tag{1}$$

$$\frac{\partial (\bar{\rho}\tilde{u_i})}{\partial t} + \frac{\partial}{\partial x_j}[\bar{\rho}\tilde{u_i}\tilde{u_j} + \bar{p}\delta_{ij} - \bar{\tau_{ij}} + \tau^{sgs}] = \tilde{F}^{s,i} \tag{2}$$

$$\frac{\partial (\bar{\rho}\tilde{E})}{\partial t} + \frac{\partial}{\partial x_j}[(\bar{\rho}\tilde{E}\tilde{p})\tilde{u_j} + \bar{q_j} - \tilde{u_i}\bar{\tau_{ij}} - H_j^{sgs} + \sigma_j^{sgs}] = \tilde{Q}^s \tag{3}$$

$$\frac{\partial (\bar{\rho}\tilde{Y_k})}{\partial t} + \frac{\partial}{\partial x_j}[\bar{\rho}\tilde{U_i}\tilde{Y_k} + J_{i,k} + Y_{i,k}^{sgs}] = \bar{\dot{\omega}}_k + \tilde{S}^s \tag{4}$$

The spatially filtered variables are denoted as $\bar{f}$, and Favre-averaged variables as $\tilde{f} = \bar{\rho f}/\bar{\rho}$. The filtered viscous stress tensor and heat flux vector are $\bar{\tau}_{ij}$ and $\bar{q}_i$ respectively. Y_k refers to the mass fraction of the k_{th} species. The species diffusion flux is denoted as J. The unresolved sub-gris scale "sgs" terms in 2 and 3, including the stress τ_{ij}, the energy flux H_j, and the viscous work σ_j, are given as:

$$\tau_{ij}^{sgs} = (\overline{\rho u_i u_j} - \overline{\rho}\tilde{u_i}\tilde{u_j}) \tag{5}$$

$$H_i^{sgs} = (\overline{\rho E u_i} - \overline{\rho}\tilde{E}\tilde{u_i}) + (\overline{pu_i} - \overline{p}\tilde{u_i}) \tag{6}$$

$$\sigma_i^{sgs} = (\overline{u_j \tau_{ij}} - \tilde{u_j}\tilde{\tau_{ij}}) \tag{7}$$

The algebraic version of the Smagorinsky model suggested by Erlebacher et al. [10] is used to close the sgs shear stress τ_{ij}^{sgs}. Flow inhomogeneities near the wall are treated using the Van Driest damping function.

Multi-phase modelling

The dispersed-phase dynamics is modeled using a Lagrangian approach. Since tracking every droplet is a computationally expensive process, multiple droplets of identical size, location, velocity and temperature are clustered together and treated as parcels. The motion of a individual parcels are then determined by Newton's second law of motion as follows:

$$\frac{dx_d}{dt} = u_d,\ m_d\frac{du_d}{dt} = F_d \tag{8}$$

where x_d is the instantaneous particle location, and m_d the mass. The subscript "d" is used for droplets. Only the force arising from skin friction and form drag is taken into account, after neglecting the contributions from virtual mass, buoyancy, Basset forces, gravity, and lift..

$$F_d = \frac{1}{8}C_D\rho_g\pi {d_p}^2|u_R|u_R \tag{9}$$

d_p and u_R are the particle diameter and velocity relative to the surrounding carrier fluid, respectively. The drag coefficient for a sphere C_D is determined based on the empirical correlation by

$$C_D = \begin{cases} \frac{24}{Re_d}(1+\frac{{Re_d}^{2/3}}{6}) & Re_d < 1000 \\ 0.424 & Re_d \geq 1000 \end{cases}$$

where Re_d is the particle Reynolds number based on the relative velocity. The droplet mass transfer is governed by the droplet continuity equation:

$$\frac{dm_d}{dt} = -\dot{m}_d = \dot{m}^s \tag{10}$$

where m_d is the mass of the droplet given by $\frac{4}{3}\rho_d\pi r_d^3$, and $\dot{m}_d(>0)$ is the net mass transfer rate (or vaporization rate) for a droplet in a convective flow field, expressed as

$$\frac{\dot{m}_d}{\dot{m}_{d,Re_d=0}} = 1+\frac{0.278{Re_d}^{1/2}{S_c}^{1/3}}{1+\frac{1.232}{Re_dSc^{4/3}}} \tag{11}$$

where $Re_d = 0$ is the Reynolds number for particle at rest.

Droplet heat transfer is governed by the droplet energy equation, which accounts for the convective heat transfer between the droplet and the surrounding air, and the latent heat of vaporization of the droplet. Temperature is assumed to be uniform throughout the droplet. The equation governing the internal temperature distribution now looks as:

$$m_dC_l\frac{dT_d}{dt} = \dot{Q_{conv}} - \dot{m}_dL_v = h_d\pi d_d^2(\tilde{T}-T_p) - \dot{m}L_v \tag{12}$$

$$\frac{\dot{h}_d}{\dot{h}_d,Re_d=0} = 1+\frac{0.278{Re_d}^{1/2}Pr^{1/3}}{1+\frac{1.232}{Re_dPr^{4/3}}} \tag{13}$$

where $\dot{Q_{conv}}$ is the convective thermal energy transfer rate, C_l is liquid heat capacity, h_d is the heat transfer coefficient, and L_v is the latent heat of vaporization. Additional details of this model, including the heat transfer coefficient and the latent heat of vaporization, can be referred to elsewhere [11].

Spray closure models

Hydrodynamic stability analysis developed by Reitz [12] is implemented to model liquid injection and primary atomization. The disintegration of liquid jet is modeled by injecting liquid in the form of "blobs", instead of an intact liquid jet at the nozzle exit. Each blob has a characteristic size equal to the injector exit diameter, d_o , that is, $d_{int} = d_o$. The number of blobs injected per unit time is determined from the injector mass flow rate. Each blob is assigned an initial radial velocity component $V_o = U_o tan(\theta/2)$, where U_o is the injection velocity, and the spray angle θ is assumed to be uniformly distributed between 0 and ϕ, with

$$tan(\theta/2) = A_1\Lambda\omega/U_o \tag{14}$$

where A_1 is 0.188 for a sharp entrance nozzle with a length to diameter ratio of 5. By invoking the effects of Kelvin-Helmholtz (K-H) instability in jets, the frequency of the fastest growing K-H wave ω, and the corresponding wave length, λ, is determined using a curve-fit solution of the linearized hydrodynamic equations as follows:

$$\frac{\Lambda}{a} = 9.02\frac{(1+0.45Z^{0.5})(1+0.4T^{0.7})}{(1+0.87{We_g}^{0.67})^{0.6}} \tag{15}$$

$$\omega\frac{\rho_l a^3}{\sigma} = 9.02\frac{(0.34+0.38{We_g}^{1.5})}{(1+Z)(1+1.4T^{0.6})} \tag{16}$$

where $Z = {We_l}^{0.5}/Re_l$ is the Ohnesorge number, $We_l = \rho_l U_R a/\sigma$ the liquid Weber number, $We_g = \rho_g U_r d/\sigma$ the gas Weber number, and $T = ZWe_2{}^{0.5}$ the Taylor number. The variable a is the blob/parent droplet radius. The subscripts l and g denote the liquid and gas phases, respectively.

Breakup of liquid droplets moving in a gaseous environment is assumed to be caused by aerodynamic liquid-gas interactions, i.e., shear-flow and drag-deceleration induced instability waves. The droplets are modeled such that their size is proportional to the wavelength of the fastest growing surface-instability wave, given as :

$$r = B_oA(B_o\Lambda < a) \tag{17}$$

$$r = min[(3/\pi a^2W/2\omega)^{0.33}(3a^2\lambda/4)^{0.34}](B_o\lambda > a) \tag{18}$$

where B_0 is a constant and equals 0.61. Once the parent droplet breaks up, the new droplets are now tracked, and the mass lost by the original droplet after the breakup is assigned to the child droplets. The rate of change of drop radius in a parent parcel is assumed to obey the following equation:

$$\frac{da}{d\tau} = -\frac{a-r}{\tau} \tag{19}$$

where $\tau = 3.726B_1a/\lambda\omega$, with B_1 being a breakup time constant, and is set to a value of 1.73 as recommended by Liu et al. [8]. The Taylor Analogy Breakup (TAB) model [13], is used to model secondary atomization. More information may be found in Khare et al. [14].

Finally, the impingement of droplets on solid surfaces(walls) is treated as recommended by Mundo et. al [15]

Coupling between dispersed and carrier phase

Coupling between the dispersed phase and the gas phase are provided by the inter-phase exchange terms or the source terms that appear on the right-hand side of the governing equations. These are computed as follows :

$$\begin{pmatrix} \dot{\rho}_s \\ \dot{F}_s \\ \dot{Q}_s \\ \dot{S}_{i,s} \end{pmatrix} = \begin{pmatrix} \sum_m n_d \dot{m}_d \\ \sum_m n_d [\dot{m}_d u_d - \frac{4\pi}{3} \rho_d {r_d}^3 \frac{du_d}{dt}] \\ \sum_m n_d [\dot{m}_d h_{v,s} - h_d \pi {d_d}^2 (T - T_d) - u_d m_d . \frac{d(u_d)}{dt} + \dot{m}_d (\frac{1}{2} u_d . u_d)] \\ \sum_m n_d \dot{m}_d \end{pmatrix} \quad (20)$$

where the summation index m is over all of the droplet "computational parcels", as defined earlier, crossing a computational cell volume. It must be noted that the species source term $\dot{S_{i,s}}$ for all species is zero, except for vaporizing fuel. Additional source terms due to combustion are computed separately, details of which can be referred to in [16]

The governing equations that are solved for the gaseous phase, as described in the previous section, are solved using a finite volume method employed on a structured grid. Spatial discretization is second-order accurate, and central-differencing scheme is used in generalized coordinates. A fourth-order matrix dissipation, with a total-variation-diminishing method is applied to ensure computational stability and prevent numerical oscillations in regions with steep gradients. Temporal discretization is obtained using a four-step Runge-Kutta integration scheme. Multi-block domain decomposition is used to facilitate the implementation of paral-lel computation with message passing interfaces at the domain boundaries.

MODEL VALIDATION

First, the theoritical framework and numerical methods developed as a part if this effort are validated against measurements of Stenzler et al. [17] for both non-vaporizing and vaporizing water jets in air crossflow. Figure 1 shows the schematic of the computational setup and the grid used for the calculation. The operating conditions and associated non - dimensional quantities are listed in table 1 fot the two cases - one with ambient air temperature of 300 K (non - vaporizing) and the one other at T = 573 K (vaporizing). The injector exit diameter is 0.254 mm, through which water is injected into the domain. For both cases, the Weber number and momentum flux ratio are fixed to 68 and 9 respectively. The grid is particularly well refined, with a densely packed grid in the near-field of the injector. Such refinement is necessary to be able to account for the effect of the finite-size of the injected droplet. Also, a well refined grid is required to capture the unsteady wake that is generated downstream of the injected jet. The smallest grid size chosen is 0.02 mm (in both X and Z direction), such that there are at least 10 grid points within the diameter of the jet, which ensures that the shape of the droplet is resolved. Such a dense grid is retained upto a distance of 12 injector diameters (3 mm) downstream of the injector location, as well as 1.6 injector diameters (0.4 mm) in the Z direction. The grid is gradually stretched away from the jet, and is once again refined close to the walls of the test section. A total of 8.4×10^6 grid points are used to mesh the whole computational domain. The jet Reynolds number is calculated to be 2059, and the grid refinement required based on the estimated Taylor microscale was found to be less stringent than that chosen above. The grid chosen above is therefore conservative.

TABLE 1: Initial conditions for gas phase and liquid phase for the two validation cases

Flow condition		
T_a (K)	300	573
u_a (m/s)	116	166
u_j (m/s)	12.01	12.36
ρ_a (kg/m^3)	1.18	0.62
σ (N/m)	7.28e-2	7.28e-2
μ_a (Ns/m^2)	1.86e-5	2.98e-2

Case	V_1	V_2
q	9	9
We	68	68.3
Re	2059.3	933.7

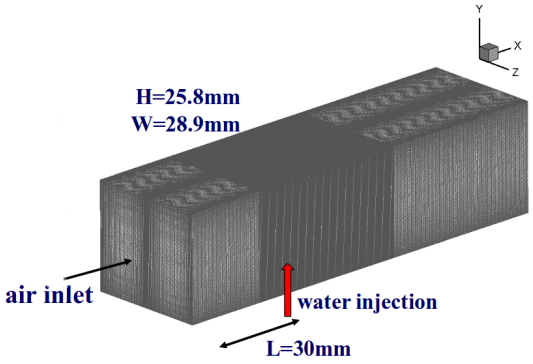

FIGURE 1: Schematic of the jet in crossflow setup

Fig. 2 shows the comparison of jet penetration obtained in the present simulations with experiments. For both the cases, the penetration depth is predicted well in comparison with correlations developed by Stenzler et al. [17]. Figure 3 shows the sauter mean diameter (SMD) distribution at 4 stations for both the cases. The expansion of the jet core is evident from the

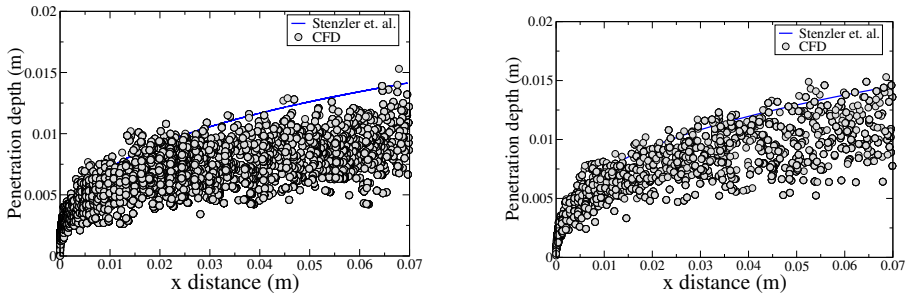

(a) T_a = 300K (b) T_a = 573K

FIGURE 2: Comparison of predicted jet penetration with experimental correlations

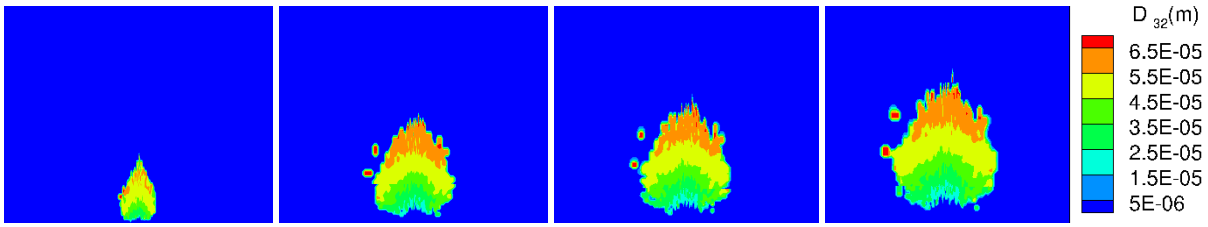

(a) x = 1 mm (b) x = 9 mm (c) x = 18 mm (d) x = 25.4 mm

FIGURE 3: SMD distribution on the y-z plane at progressive streamwise locations showing the development of the spray field at T_a = 300 K.

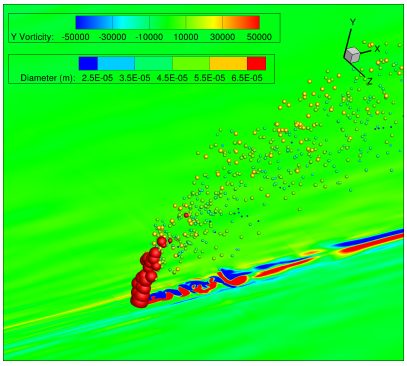

FIGURE 4: An instantaneous contour of Y - vorticity showing the presence of strong unseady wake vortices downstream of the jet

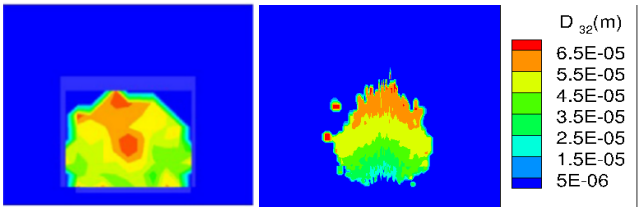

(a) experiment (b) present calculation

FIGURE 5: Comparison of SMD distribution for case V_1, at x=25.4 mm from the inlet

increasing area over which the droplets are distributed moving downstream. The largest droplets (55 - 65 μm) appear to be concentrated at the edges in the upper region of the jet, with mid-sized droplets distributed (35 - 55 μm) largely present at the center of the jet core. Relatively smaller droplets are distributed closer at the bottom.

Fig 5 shows the comparison of the SMD distribution for this case at x = 25.4 mm with experimental observations made by Stenzler et.al. [17]. The trends and the global droplet size distribution are in good agreement. One significant deviation seen in the present results, in comparison with experiments is that while larger sized droplets are present in the center of the jet core, the present simulation predicts these droplets to be present mostly close to the upper edge of the jet core. While carrying out the simulations, it was noted that capturing the wake shed behind the injected jet was critical for correctly estimating the spreading of the jet, and hence the droplet distribution. Fig 4 shows an instantaneous vorticity contour, that clearly shows the counter-rotating wake vortices shed downstream of the jet.

EFFECT OF MOMENTUM FLUX RATIO

To identify the effect of momentum flux ratio, q on the spatio-temporal behavior of gaseous and spray dynamics in jet in vitiated cross flow configuration, high-fidelity numerical calculations are conducted for a range of q from 10-140. The working fluids are air and water. The operating conditions consist of p = 1 atm, incoming air velocity of 141.4 m/s at a temperature of 600K. Table 2 shows the operating condition and the corresponding non-dimensional quantitites. Detailed results are presented for momentum flux ratios of 10, 30 and 140. Momentum flux ratio is defined as $q = \rho_j u_j^2 / \rho_a u_a^2$, and the Weber number as $We = \rho_a u_{rel}^2 D/\sigma$, where u_{rel} is defined as $u_{rel} = |u_a - u_j|$. Reynolds number is calculated based on inflow velocity and width of the v-gutter 'a',which may be expressed as $Re = \rho_a u_a a/\mu_a = 29425$. This Reynolds number is larger than the one based on the jet diamater, and hence the grid refinement is done based on the flow Reynolds number in this case. Figure 6 shows the schematic of the physical setup. Water is injected 40 mm downstream of the inlet. A triangular bluff body is placed 140 mm from the inlet, with an equilateral cross section of side length 10 mm. The configuration for this setup is shown in fig 6. The bluff body placed in the jet stream has an equilateral triangular cross-section with side length of 10 mm.

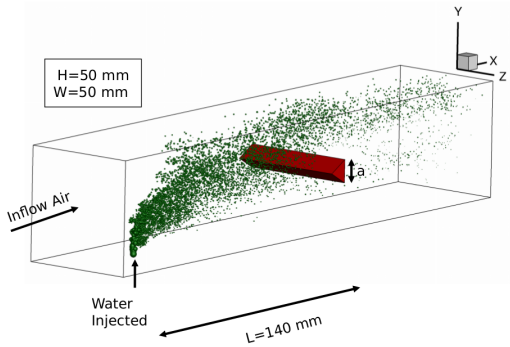

FIGURE 6: A schematic of the flow configuration

Based on the Reynolds number, 7.4×10^6 grid points are used to discretize the computational domain. Grid is well resolved in the boundary layer region close to the duct walls, as well as wall surfaces on the bluff-body. 132 grid points each are used in the two wall-normal directions. 240 grid points are present in the streamwise direction upstream of the bluff-body, and 180 points downstream of it. Grid is particularly well resolved in the near-field region of injected jet and in the wake region of the bluff-body. The smallest grid size is 0.1 mm, closest to the wall surface of the bluff-body, sufficient to capture the thickness of the boundary layer.

TABLE 2

	Flow condition
T_a (K)	600
u_a (m/s)	141.3
u_j (m/s)	10.86
ρ_a (kg/m^3)	0.588
σ (N/m)	7.28e-2
μ_a (Ns/m^2)	3.01e-5

Case	A	B	C	D
q	10	30	50	140
We	162.21	164.12	166.02	172.51
Re	29425	29425	29425	29425

Gas phase flow physics

Figure 7 shows an instantaneous snapshot of the turbulent flowfield that is established when a liquid jet is injected into incoming air at high temperature. In general, due to intense exchange of momentum and energy between the jet column and the freestream, there is a velocity deficit in the wake of the jet. This interaction also increases the unsteadiness of freestream air. An unsteady wake is seen behind the bluff-body.

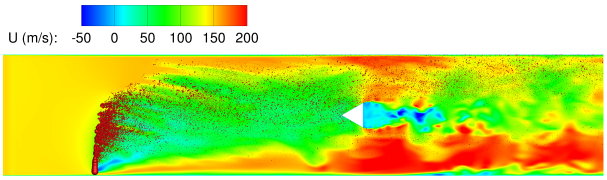

FIGURE 7: A representative instantaneous visualization of the flow field for the liquid jet interacting with crossflowing air

Figure 8 shows contours of time-averaged mass fraction of vaporized water in the gas-phase for cases A, B and D corresponding to momentum flux ratio of 10, 30 and 140 respectively. The contours are shown on cross-sectional planes at 4 streamwise locations of 80 mm, 120 mm, 170 mm and 210 mm from the inlet. In case A, water vapour is mostly concentrated close to the bottom wall of the test section. With increase in jet velocity, in case B, vapor concentration encompasses a larger region due to better spreading of the jet core. For case C, due to an even larger velocity, most of the liquid droplets are concentrated close to the upper wall of the test section, which explains the high concentration of water vapor in that region. In all cases, water is seen to diffuse over a larger region as it convects downstream.

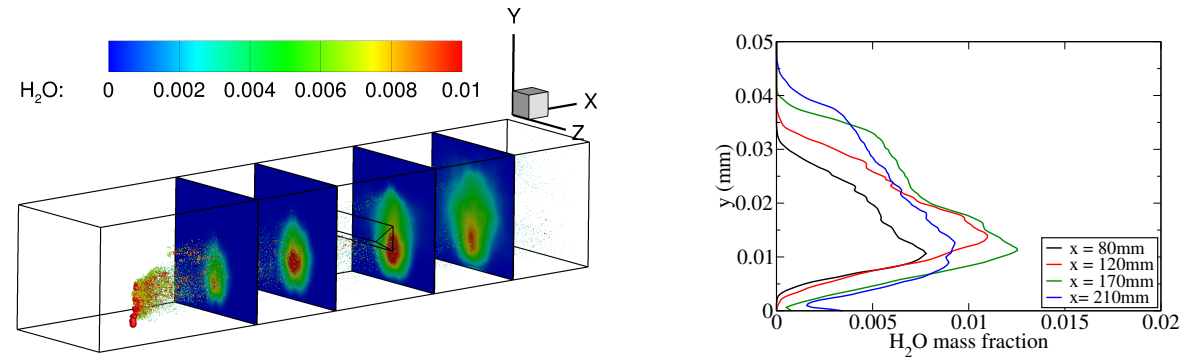

(a) case A, q = 10

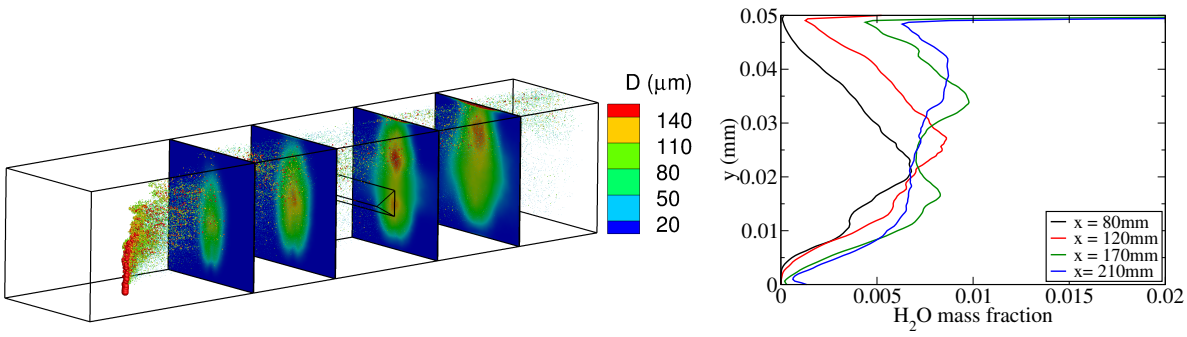

(b) case B, q = 30

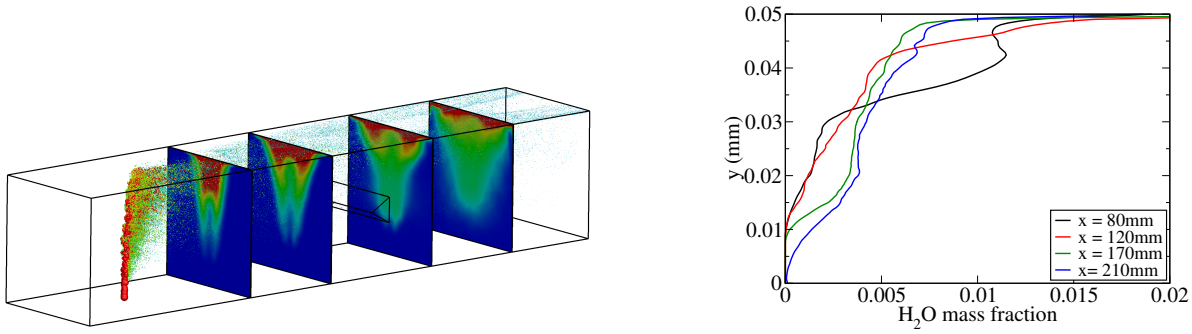

(c) case D, q = 140

FIGURE 8: Contours of time - averaged mass fraction of vaporized H_2O in the gas phase, and plots showing the trend in its variation for the corresponding cases at streamwise locations x = 80 mm, x = 120 mm, x = 170 mm and x = 210 mm.

These trends are more apparent in figure 9 that shows profiles of water vapor mass fraction at the mid-plane (z = 25 mm) at different streamwise locations.

Figure 9 shows contours of streamwise velocity for the three cases considered here. Once again, contours are shown at the same streamwise locations as before, namely x = 80 mm, 120 mm, 170 mm and 210 mm. Contours at stations x = 80 mm and x = 120 mm clearly show momentum deficit for air in the wake of the liquid jet in all cases. Profiles of average streamwise velocity at these stations confirm the observation. However, velocity contour in the wake of the V-gutter (x = 170 mm) looks different for case B compared to other cases, and shows a larger velocity deficit away from the mid - plane in z direction. To investigate

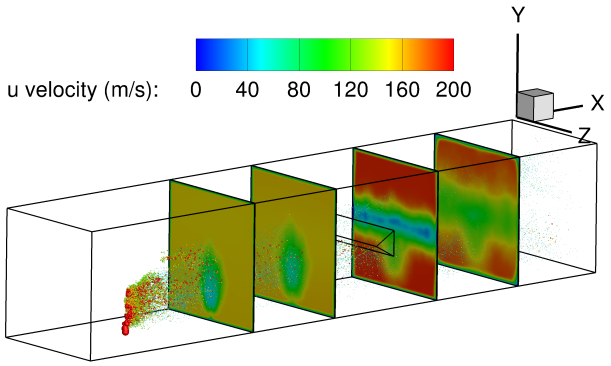

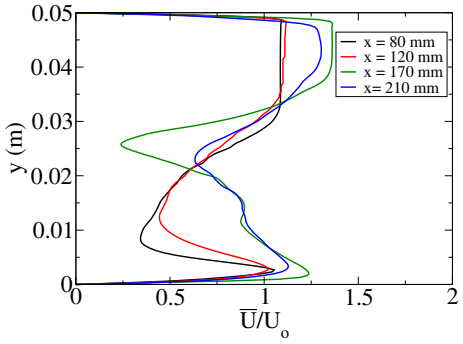

(a) case A, q = 10

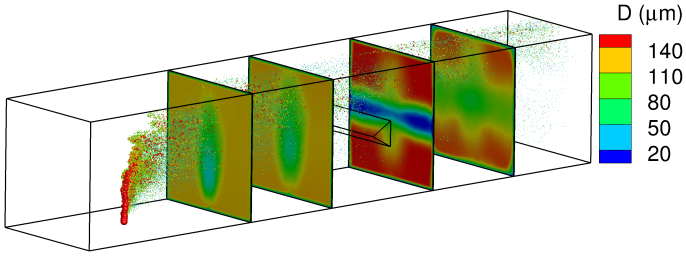

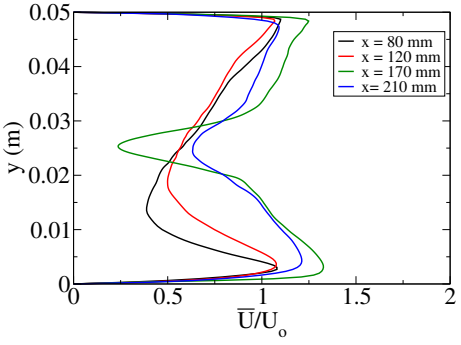

(d) case B, q = 30

(b) case B, q = 30

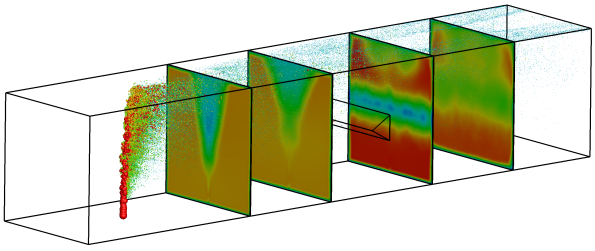

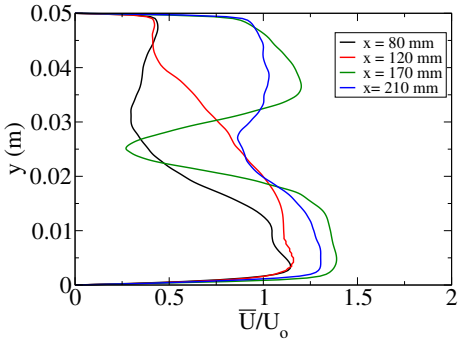

(c) case D, q = 140

FIGURE 9: Contours of time - averaged streamwise velocity, and plots showing the trend in its variation for the corresponding cases at streamwise locations x = 80 mm, x = 120 mm, x = 170 mm and x = 210 mm.

this aspect further, variation of streamwise velocity from the bottom to top wall at a section 10 mm from the side wall is shown in figure 10 (a) (z = 10 mm). A large velocity deficit at the center (y = 25 mm) for case B indicates the presence of a stronger wake behind the bluff-body compared to other cases. Larger magnitude of normal velocity, as seen in figure 10 (b) also suggests the presence of a highly unsteady wake for case B. Finally, figure 10 (c), shows high vorticity content for case B, further providing evidence for the presence of a strong wake. A strong wake for case B may be attributed to the influence of dispersed droplets.

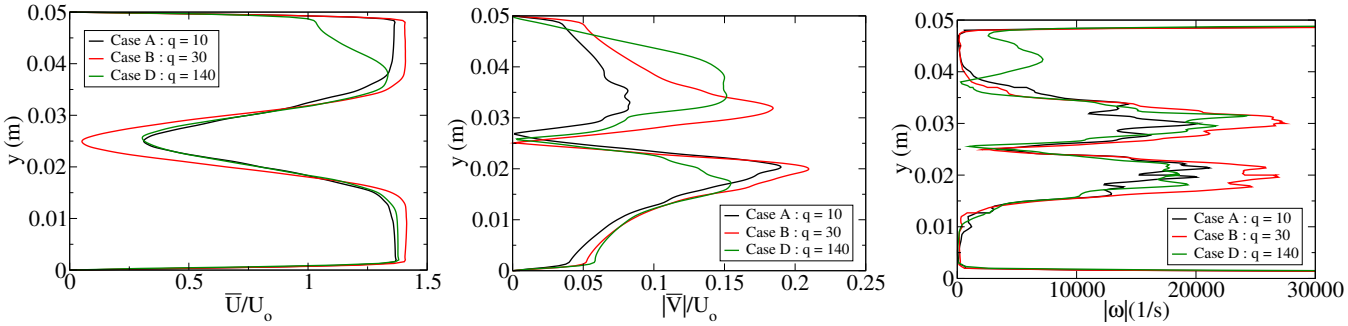

FIGURE 10: Plots of (a) streamwise velocity (b) magnitude of normal velocity and (c) vorticity magnitude at a location behind the bluff body (x = 170 mm) and 10 mm away from the side wall (z = 10 mm) indicating presence of a stronger wake for case B as compared to other cases.

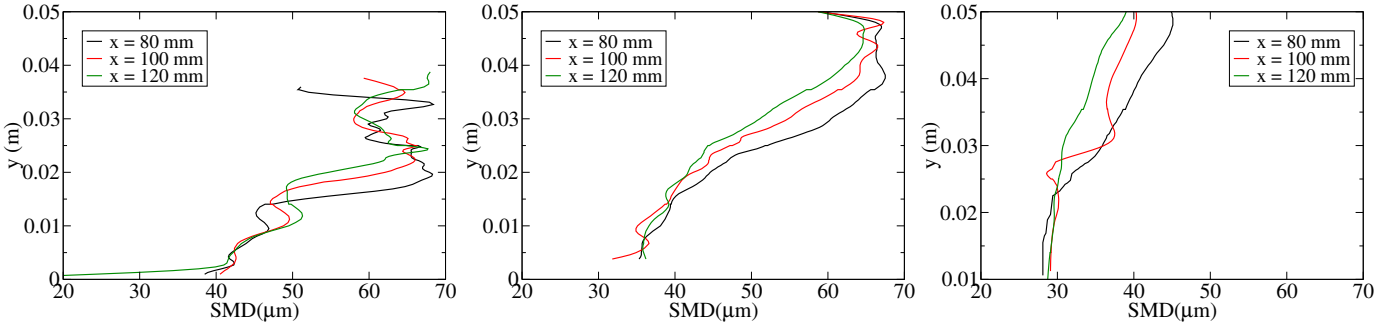

(a) case A, q = 10 (b) case B, q = 30 (c) case D, q = 140

FIGURE 11: Plots of variation of sauter mean diamater for cases A, B and D at three sample streamwise locations.

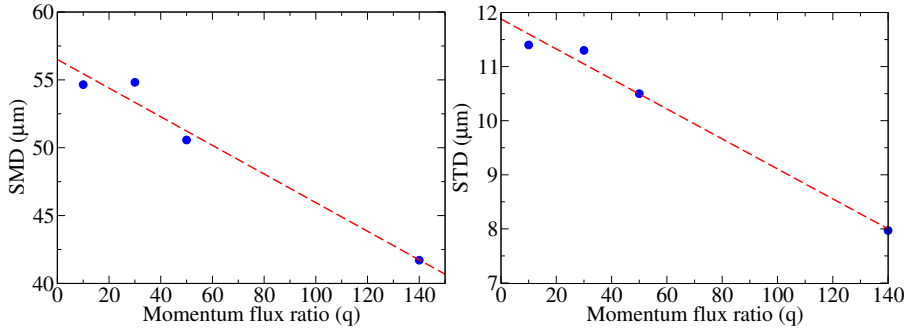

(a) Sauter Mean Diameter (SMD) vs q (b) Standard Deviation(STD) vs q

FIGURE 12: Plots of variation of global droplet sizes and standard deviation of the sizes with increasing momentum flux ratio show a general declining trend.

The core of the jet, which is mostly concentrated in the middle of the test section, constricts the effective area available for passage of air, thus causing flow acceleration. The increased air velocity leads to a stronger wake behind the bluff-body. While this effect may be expected for other cases as well, the core of the jet is either concentrated closer to the bottom wall or the top wall of the test section, far enough from the bluff-body, thus reducing its prominence.

Spray dynamics and droplet statistics

Next, droplet size distributions are compared for the cases A, B and D. Variation of the sauter mean diameter (SMD) from the bottom to the top wall of the test section are presented at three streamwise locations on the mid plane (z = 25 mm) namely, x = 80 mm, x = 100 mm and x = 120 mm from the inflow plane. In figure 11, for case A, droplet sizes seem to vary from $40\mu m$ to $70\mu m$. From the bottom to top of the section, a significant non-uniformity in droplet sizes is observed, with the largest droplets present close to 20 mm from the bottom wall. In case B, the SMD increases monotonically, from bottom to the top. For case D, the SMD is distributed more uniformly. With increase in jet velocity, the exposure of the jet to freestream air increases, leading to a more uniform atomization. This explains the trend of increasing uniformity in droplet sizes with an increase in jet velocity.

Figure 12 (a) shows the global SMD (computed from 60 mm to 100 mm downstream of the location of the injector) at each of the cases of momentum flux ratio. A generally declining trend is observed. Such a trend of declining droplet size with increased jet velocity was also observed by Amighi et. al [2]. It was observed in the simulations that with increasing momentum flux ratio, a larger percentage of droplets underwent secondary atomization, thus causing the mean diameter to reduce. This can also be interpreted as an improved uniformity in atomization. A declining standard deviation of droplet size with increase in momentum flux ratio, as seen in figure 12 (b) is a statistical evidence to further support this claim.

CONCLUSION

High fidelity simulations were conducted to analyse the effect of momentum flux ratio on the gaseous and spray dynamics of water jet injection in hot crossflowing air, with a v-gutter bluff-body placed downstream. For all the cases, the Reynolds number was fixed at 29425, while the Weber number and momentum flux ratio was varied from 162.2 - 172.5 and 10 - 140 respectively.

Mean contours of vapor fraction of water, as well as sreamwise velocity were shown at select streamwise stations for increasing momentum flux ratio. While a velocity deficit was observed in the wake of the spray field in all cases, the wake behind the v-gutter was more enhanced for the case of q = 30. This was due to the presence of the jet core close to the bluff body, thus causing air to accelerate within the constricted passage, and leading to an enhanced wake.

With increasing momentum flux ratio, the droplet size distribution was observed to vary more uniformly. Also, a gradual drop in the mean droplet size was observed with increase in momentum flux ratio. It was explained that with an increase in momentum flux ratio, the liquid jet was exposed to freestream air better, over a larger surface area, and thus promoting an enhanced breakup and atomization of the jet column, leading to uniform mixing as well as smaller droplet sizes.

REFERENCES

[1] Wu, P.-K., Kirkendall, K. A., Fuller, R. P., and Nejad, A. S., 1997. "Breakup Processes of Liquid Jets in Subsonic Crossflows". *Journal of Propulsion and Power,* ***13***(1), pp. 64–73.

[2] Amighi, A., and Ashgriz, N., 2018. "Global Droplet Size in Liquid Jet in a High Temperature and High Pressure Cross Flow". In 2018 AIAA Aerospace Sciences Meeting, no. January, American Institute of Aeronautics and Astronautics, pp. 1–17.

[3] Tambe, S., Jeng, S.-M., Mongia, H., and Hsiao, G., 2005. "Liquid Jets in Subsonic Crossflow". In 43rd AIAA Aerospace Sciences Meeting and Exhibit, no. January, American Institute of Aeronautics and Astronautics, pp. 1–12.

[4] Kihm, J. D., Lyn, G. M., and Son, S. Y., 1995. "Atomization of cross-injecting sprays into convective air stream". *Atomization and Sprays,* ***5***, pp. 417–433.

[5] Becker, J., and Hassa, C., 2002. "Breakup and atomization of a kerosene jet in crossflow at elevated pressure". *Atomization and Sprays,* ***12***, pp. 49–67.

[6] Oh, J., Lee, J. G., and Lee, W., 2013. "Vaporization of a liquid hexanes jet in cross flow". *International Journal of Multiphase Flow,* ***57***, dec, pp. 151–158.

[7] Brandt, M., Rachner, M., and Schmitz, G., 1998. "An Experimental and Numerical Study of Kerosine Spray Evaporation in a Premix Duct for Gas Turbine Combustors at High Pressure". *Combustion Science and Technology,* ***138***(1-6), sep, pp. 313–348.

[8] Liu, A. B., Mather, D., and Reitz, R. D., 1993. Modeling the effects of drop drag and breakup on fuel sprays. Sae technical paper, Mar.

[9] Madabhushi, R. K., Leong, M. Y., and Hautman, D. J., 2004. "Simulation of the Break-Up of a Liquid Jet in Crossflow at Atmospheric Conditions". In Volume 1: Turbo Expo 2004, ASME, pp. 697–704.

[10] Erlebacher, G; Hussaini, M. Y.; Speziale, C. G.; Zang, T. A., 1992. "Toward the Large-Eddy Simulation of Compressible Turbulent Flows". *Journal of Fluid Mechanics,* ***238***, pp. 155–185.

[11] Faeth, G. M., 1983. "Evaporation and combustion of sprays". *Progress in Energy and Combustion Science,* ***9***(1-2), pp. 1–76.

[12] Reitz, R. D., 1987. "Modeling atomization processes in

high-pressure vaporizing sprays". *Atomization and Spray Technology,* ***3***, pp. 309–337.

[13] O'Rourke, P., and Amsden, A., 1987. The tab method for numerical calculation of spray droplet breakup. Sae technical paper 872089, Nov.

[14] Khare, P., Wang, S., and Yang, V., 2015. "Modeling of finite-size droplets and particles in multiphase flows". *Chinese Journal of Aeronautics,* ***28***(4), pp. 974–982.

[15] Mundo, C., Sommerfeld, M., and Tropea, C., 1995. "Droplet-wall collisions: Experimental studies of the deformation and breakup process". *International Journal of Multiphase Flow,* ***21***(2), pp. 151–173.

[16] Kamin, M., and Khare, P. Combustion of kerosene jet injected into crossflowing air. under preparation.

[17] Stenzler, J. N., Lee, J. G., Santavicca, D. A., and Lee, W., 2006. "Penetration of Liquid Jets in a Cross-Flow". *Atomization and Sprays,* ***16***(8), pp. 887–906.